

QUASARS: WHAT TURNS THEM OFF?

ROBERT J. THACKER^{1,2}, EVAN SCANNAPIECO³, AND H. M. P. COUCHMAN⁴

(Received; Accepted)
Draft version April 25, 2018

ABSTRACT

While the high-redshift quasar luminosity function closely parallels the hierarchical growth of dark matter halos, at lower redshifts quasars exhibit an anti-hierarchical turn-off, which moves from the most luminous objects to the faintest. We explore the idea that this may arise from self-regulating feedback, caused by quasar outflows. Using a detailed hydrodynamic simulation we calculate the luminosity function of quasars down to a redshift of $z = 1$ in a large, cosmologically representative volume. Outflows are included explicitly by tracking halo mergers and driving shocks into the surrounding intergalactic medium, with an energy output equal to a fixed 5% fraction of the bolometric luminosity. Our results are in excellent agreement with measurements of the spatial distribution of quasars on both small and large scales, and we detect an intriguing excess of galaxy-quasar pairs at very short separations. Our results also reproduce an anti-hierarchical turnoff in the quasar luminosity function, however, this falls short of that observed as well as that predicted by analogous semi-analytic models. The difference can be traced to the treatment of heating of gas within galaxies and the presence of in-shock cooling. Calculations of the mass fraction of gas above the critical entropy show a strong redshift dependence with close to 20% of the baryons being above this limit at $z = 1$. Volume fractions show an even stronger trend with redshift and some sensitivity to resolution due to the tendency of high entropy gas to occupy low density regions. The simulated galaxy cluster $L_X - T$ relationship is close to that observed for $z \approx 1$ clusters, but the simulated galaxy groups at $z = 1$ are significantly perturbed by quasar outflows, suggesting that measurements of X-ray emission in high-redshift groups could well be a “smoking gun” for the AGN heating hypothesis.

Subject headings:

1. INTRODUCTION

In the low-redshift universe, active galactic nuclei (AGN) are not very active. While at high redshifts, the quasar luminosity function increases with time, since $z \approx 2$ the number density of optically-selected AGN has been dropping dramatically (Schmidt & Green 1983; Boyle *et al.* 1988 Koo & Kron 1988; Pei 1995; Boyle *et al.* 2000; Fan *et al.* 2001). Deep X-ray surveys have shown that this downturn occurs anti-hierarchically, such that the spatial density of AGN with higher X-ray luminosities peaks earlier than that of lower-luminosity AGN (Steffen *et al.* 2003; Ueda *et al.* 2003). Complementary emission line studies suggest that this trend is driven by a decrease in the characteristic mass of actively growing black holes (Heckman *et al.* 2004), and is likely to closely parallel the formation history of early-type galaxies (*e.g.* Granato *et al.* 2001, 2004). Furthermore, optical and near-infrared observations indicate that the largest galaxies were already in place by $z \approx 2$, while smaller ones continued to form stars at much lower redshifts (Pozzetti *et al.* 2003; Fontana *et al.* 2004; Glazebrook *et al.* 2004; van Dokkum *et al.* 2004; Treu *et al.* 2005), and a similar trend is observed in the morphological evolution of galaxies (Bundy, Ellis, & Conselice 2005).

Yet, despite these observations, such widespread

galaxy “downsizing” (Cowie *et al.* 1996) was unexpected. The Λ Cold Dark Matter (Λ CDM) model, while in spectacular agreement with observations (*e.g.* Spergel *et al.* 2003), is a hierarchical theory, in which gravitationally-bound structures grow by accretion and merging. Superimposed on this distribution is the baryonic component, which falls into the dark-matter potential wells, shock heats, and must radiate this energy away before forming stars (Rees & Ostriker 1977; Silk 1977). The larger the structure, the longer it takes to cool, and thus galaxy evolution should be even more hierarchical than structure formation.

Recently, several theoretical studies have shown that the missing element in this picture could be kinetic feedback from AGN. As bulge and black hole masses are closely related (Gebhardt *et al.* 2000; Merritt & Ferrarese 2001; see also King 2003, 2005), such outflows would have the largest impact on the largest forming elliptical galaxies, suppressing their formation first (Scannapieco & Oh 2004, hereafter SO04; Binney 2004; Di Matteo *et al.* 2005; Croton *et al.* 2006). This would also help to explain the X-ray luminosity-temperature relationship observed in the intracluster medium (ICM) in galaxy clusters. If nongravitational heating were unimportant, the gas density distribution would be self-similar, resulting in $L_X \propto T^2$ (Kaiser 1986), but instead the observed slope steepens considerably for low-temperature clusters (*e.g.* David *et al.* 1993; Arnaud & Evrard 1999; Helsdon & Ponman 2000). Furthermore the 100 keV cm² level of preheating necessary to explain this discrepancy (Cavaliere *et al.* 1998; Kravtsov & Yepes 2000; Wu *et al.* 2000; Babul *et al.* 2002) is not arbitrary. Rather it corresponds

¹ Department of Physics, Engineering Physics and Astronomy, Queen’s University, Kingston, Ontario, K7L 3N6, Canada.

² CITA National Fellow

³ Kavli Institute for Theoretical Physics, Kohn Hall, University of California, Santa Barbara, CA 93106

⁴ Department of Physics and Astronomy, McMaster University, 1280 Main St. West, Hamilton, Ontario, L8S 4M1, Canada.

to the threshold value for cooling within the age of the universe (Voit & Bryan 2001; Oh & Benson 2003).

Taken together, these observations are strongly suggestive of a model in which the properties of the ICM, the formation history of elliptical galaxies, and the evolution of the quasar luminosity function are all set by self-regulating AGN feedback. In fact, S004 have shown that the addition of AGN outflows into the semi-analytic model developed by Wyithe & Loeb (2002; 2003) can reproduce the drop in the AGN luminosity at low redshifts, as heating this gas slows the accretion of matter onto the supermassive black hole. The central AGN engine is then starved of fuel and a strong suppression at the bright end of the luminosity function occurs. The main drawback of the model, however, is that precise matching of observational results requires fine tuning of the model parameters, such as black hole mass and outflow efficiency.

Several other recent numerical and analytic investigations have sharpened our understanding of various aspects of this process. Binney (2004) conducted an analytic study of the impact of AGN on inhibiting gas cooling in large galaxies. Di Matteo *et al.* (2005) carried out Smoothed Particle Hydrodynamic (SPH) simulations of AGN outflows in individual galaxy mergers and studied the role of feedback in determining the colors of elliptical galaxies and establishing the relationship between stellar velocity dispersion and black hole mass. This suite of simulations was later related analytically to the global evolution of quasars and elliptical galaxies in series of papers by Hopkins *et al.* (2005a, 2005b, 2005c, 2006). Levine & Gnedin (2005) combined cosmological simulations with an analytic model to constrain the filling factor of AGN outflows as a function of redshift. Scannapieco, Silk, & Bouwens (2005) emphasized the role that quasars may play in the downsizing of the star-forming galaxy population. Levine & Gnedin (2006) studied the impact of AGN outflows on the matter power spectrum. Menci *et al.* (2006) used a semianalytical model to study the role of AGN feedback on the color distribution of galaxies from $z = 0$ to $z = 4$. The importance of the nature of gas accretion in determining the effectiveness of feedback processes has recently been discussed in Dekel & Birnboim (2006) and Cattaneo *et al.* (2006). Finally, Croton *et al.* (2006) combined semi-analytic models with the dark-matter evolution taken from the Millennium Simulation (Springel *et al.* 2005) to study the impact of a more temporally-extended model of AGN feedback on the bright end of the galaxy luminosity function.

In this paper we undertake the first detailed hydrodynamic simulations of quasar outflows in a general cosmological context. Adopting a burst model that associates AGN with merger events and a global outflow model that is based on our simulations of high-redshift starbursts (Scannapieco, Thacker, & Davis 2001, hereafter STD01), we are able track in detail the impact that quasars have both on their own formation, and on the properties of galaxy clusters and the intergalactic medium (IGM).

The structure of this work is as follows. In §2 we describe our overall numerical approach, method for quasar identification, and implementation of outflows. In §3 we compare our simulation results with measures of quasar clustering and the observed luminosity function in the optical and the X-ray bands. In §4 we study AGN feed-

back in a more global context, examining its impact on the properties of the intergalactic and intracluster media. In §5 we present a discussion and conclusion.

2. SIMULATIONS OF QUASAR FORMATION

2.1. Overall Numerical Model

Motivated by measurements of the cosmic microwave background, the number abundance of galaxy clusters, and high-redshift supernova distance estimates (*e.g.* Spergel *et al.* 2003; Vianna & Liddle 1996; Riess *et al.* 1998; Perlmutter *et al.* 1999), we focus our attention on a Cold Dark Matter cosmological model with parameters $h = 0.7$, $\Omega_0 = 0.3$, $\Omega_\Lambda = 0.7$, $\Omega_b = 0.046$, $\sigma_8 = 0.9$, and $n = 1$, where h is the Hubble constant in units of $100 \text{ km s}^{-1} \text{ Mpc}^{-1}$, Ω_0 , Ω_Λ , and Ω_b are the total matter, vacuum, and baryonic densities in units of the critical density, σ_8^2 is the variance of linear fluctuations on the $8h^{-1} \text{ Mpc}$ scale, and n is the “tilt” of the primordial power spectrum. The Eisenstein & Hu (1999) transfer function is used throughout.

As in our earlier work (STD01), simulations were conducted with a parallel OpenMP based implementation of the “HYDRA” code (Thacker & Couchman 2006) that uses the Adaptive Particle-Particle, Particle-Mesh algorithm (Couchman 1991) to calculate gravitational forces, and the SPH method (Lucy 1977; Gingold & Monaghan 1977) to calculate gas forces. Gas densities and energies are calculated using the standard SPH smoothing kernel method (for exact details see STD01), with the kernel tuned to smooth over 52 particles; and radiative cooling is calculated using standard tables (Sutherland & Dopita 1993). We have kept the metallicity constant at $Z = 0.05$, to mimic a moderate level of enrichment in the galaxy formation process. However, this is an underestimate of the intracluster metallicity, $Z = 0.3$, which seems to be an approximately universal value to intermediate redshifts (Tozzi *et al.* 2003). Lastly, because the epoch of reionization is poorly known, and because we are primarily focusing our attention on mass scales greater than $10^{10} M_\odot$, we do not include a fiducial photoionization background in the simulation.

We also do not include the so called “ ∇h ” terms (Nelson & Papaloizou 1994, Serna *et al.* 1996, Springel & Hernquist 2002) in our implementation of SPH. This is potentially a significant concern in this investigation as we will examine gas entropy. However, tests on an expanding spherical shell problem (see STD01) using 1000 particles and no artificial viscosity or cooling, show entropy conservation to be accurate at the 6% level, while the combined gravitational and hydrodynamic energy error is around 1.5%. These findings are in broad agreement with the discussions presented in Hernquist (1993) and Springel & Hernquist (2002), where a small entropy conservation error was always accompanied by a larger energy error when integrating the evolution of the entropic function in the absence of ∇h terms. While a lower error in the entropy is desirable, for the present phenomenological investigation and given the gains we get from using a code without ∇h terms, we consider this error acceptable.

We simulated a number of different box sizes and particle numbers to quickly assess the accuracy and numerical resolution dependencies in our model. A single large simulation was then run for statistical purposes, allow-

ing us to probe the bright end of the luminosity function. The specifics of each simulation, including box size and resolution are given in Table 1. We note that attempting to simulate the formation of the very brightest end of the luminosity function with sufficient resolution to track smaller mergers is a difficult task, due to the scarcity of these objects. This is the fundamental motivation behind our progressing to a simulation with 2×640^3 particles.

2.2. Identification of Quasars

A secondary motivation of this paper is to compare the simulation results directly with semi-analytic predictions. We have therefore taken the outflow model of SO04 and adapted it to our simulation as closely as possible, although in some cases, which we highlight, it was either not possible for us to match this model exactly, or we have chosen to make well-motivated changes. For completeness, we reiterate the salient features of the SO04 model in our discussion below.

While in our previous work it was sufficient to track group mass evolution to identify star forming regions, to evaluate the quasar luminosity function it is necessary to track mergers of groups. We have used the same method as STD01 for identifying groups, which relies upon the local baryonic density field to pinpoint centers of mass, and a spherical overdensity procedure applied to identify the baryon group. From the baryon group an estimation of the total halo mass is derived by multiplying by Ω_0/Ω_b . The resulting mass distribution function is in close agreement with that derived from friends-of-friends, provided suitable limits for the baryon spherical overdensity are chosen. To track merger events we rely upon group labeling, and we label a merger as having occurred when at least 30% of the accreted mass does not come from a single massive progenitor. This procedure means that the first groups to form are also treated as merger events. For each merger event that will be tagged as a quasar we store the details including position and redshift in an output file.

Once a group has been identified as satisfying this criterion, the dynamical time associated with the cold gas disk which feeds the AGN and the mass associated with the black hole must be calculated. For a given redshift, z , and virial density $\rho_v(z)$, the implied virial radius for a group of N gas particles with mass m_g is

$$r_v = \left[\frac{Nm_g\Omega_0/\Omega_b}{4/3\pi\rho_v(z)} \right]^{1/3}. \quad (1)$$

The circular velocity is then

$$v_c = \left[\frac{4}{3}\pi G\rho_v(z)r_v^2 \right]^{1/2}, \quad (2)$$

and the dynamical time, t_d , associated with a cold disk of gas, is defined by

$$t_d = 0.055 \times r_v/v_c. \quad (3)$$

Note that in order to maintain the same relationship between outflow velocity and black hole mass as Wyithe & Loeb (2002) and SO04, we choose a slightly larger time than was used in these studies. This is because our numerical model also includes thermal energy input to establish the correct initial post-shock temperature according to eq. (7) below.

While the observed $M_{bh} - \sigma_c$ relation (Merrit & Ferrarese 2001; Tremaine *et al.* 2002) infers that the black hole mass scales as σ_c^α , where $\alpha \sim 4-4.5$, the $M_{bh} - v_c$ has a slightly steeper slope because the $v_c - \sigma_c$ is shallower than linear (Ferrarese 2002). Thus we assume an $M_{bh} - v_c$ relationship given by,

$$M_{bh} = 2.8 \times 10^8 \left(\frac{v_c}{300 \text{ km s}^{-1}} \right)^5. \quad (4)$$

Lastly, the black hole is assumed to shine at its Eddington luminosity ($1.2 \times 10^{38} \text{ ergs s}^{-1} M_\odot^{-1}$) for the dynamical time, t_d . Note that these values are slightly different than in SO04, but the overall relationship between v_c and luminosity is the same.

2.3. Outflow Implementation

Each AGN in our simulation is assumed to channel a fixed fraction fraction, ϵ_k , of its bolometric energy into a kinetic outflow. The amount of energy deposited into the outflow is then

$$E_k = 1.2 \times 10^{38} \epsilon_k \left(\frac{M_{bh}}{M_\odot} \right) \left(\frac{t_d}{s} \right) \text{ ergs}. \quad (5)$$

As in SO04, we shall adopt $\epsilon_k = 0.05$ throughout this investigation, which is consistent with other literature estimates (*e.g.* Furlanetto & Loeb 2001; Nath & Roychowdhury 2002). The majority of mass in the outflow at the resolution we can simulate will have come from material surrounding the cold gas group. Therefore, as in our previous work, we model the expanding outflow as a spherical shell outside of the virial radius of the system. While the assumption of a spherical shell is a significant oversimplification, given the bipolar nature of outflows, it is worth recalling that within the intracluster medium in galaxy clusters a bipolar outflow will still launch an ellipsoidal cocoon of shocked intracluster gas (Begelman & Cioffi 1989). Hence, we place the expanding outflow at a radius $2r_{vir}$ and re-arrange all gas below a density threshold of $2.5\rho_{vir}$ within this radius, but outside r_{vir} , into an expanding shell. The density threshold prevents us from redistributing cold gas, which is known to be very stable against incoming shocks in SPH simulations. Once we have established the amount of mass available to create the shell, M_s , the velocity of the shell, v_s , is calculated from,

$$v_s = 1.13 \left(\frac{E_k}{M_s} - Gm_g \frac{N}{N_s} \frac{\Omega_0}{\Omega_b} \sum_{i=N+1}^{N+N_s} \frac{1}{r_i} - \frac{1}{r_o} \right)^{1/2}, \quad (6)$$

where the second term on the right-hand side denotes the potential energy subtracted as particles are moved from their initial position to the shell. As in STD01, we add an additional rotational velocity component to the shell so as to preserve the angular momentum.

Note that the prefactor in eq. (6) is less than $\sqrt{2}$ as a fraction of E_k is channeled into establishing the correct post-shock temperature in the outflowing gas. This heating is particularly important since it will help determine the fraction of impacted gas that is able to cool within a Hubble time. Under the assumption that the shell behaves like a strong shock, the postshock temperature, T_s , is

$$T_s = \frac{3\mu m_p v_s^2}{16k_B} = \frac{(13.6K)v_s^2}{(1\text{km s}^{-1})^2}. \quad (7)$$

TABLE 1
SIMULATION PARAMETERS

Run	N	Box Size (Mpc)	Mass Resolution (M_\odot)	Softening Length (kpc)	Steps ($z=1$)
0400	2×40^3	$35 h^{-1}$	1.2×10^{10}	$24 h^{-1}$	1340
0800	2×80^3	$35 h^{-1}$	1.5×10^9	$12 h^{-1}$	3678
1600	2×160^3	$35 h^{-1}$	1.9×10^8	$6 h^{-1}$	5420
3200	2×320^3	$35 h^{-1}$	2.3×10^7	$3 h^{-1}$	7381 ($z=2.5$)
1020	2×640^3	$146 h^{-1}$	2.2×10^8	$9 h^{-1}$	10420 ($z=1.2$)

While the semi-analytic model in SO04 assumes that this heating applies to the galaxy as well, here we only heat the material in the outflowing shell. Our motivation for this choice is the short cooling time of gas in galactic halos and, on a secondary level, the collimated bipolar nature of the outflows. The radial expansion of the shell agrees with analytic predictions (STD01).

Since our resolution is insufficient to provide detailed knowledge of the inner structure of galaxies we implement star formation on the basis of a merger model. Following a major merger we convert 10% of gas in the galaxy into stars particles. While this method is known to be a good model of high redshift star formation in low mass halos (STD01) it does not track quiescent mode star formation which is the primary mode of star formation in the higher mass galaxy population. We emphasize that the purpose of this study is to focus on the hydrodynamic evolution of the IGM and we are not attempting to calculate a luminosity function for galaxies, instead we use them largely as a tracer population.

3. DISTRIBUTION AND EVOLUTION OF QUASARS

3.1. Quasar Clustering

In the following three subsections we study the optical properties of quasars, as quantified in the rest-frame B-band. In keeping with our previous investigations, as well as the observations in Elvis *et al.* (1994), we relate the luminosity in this band to the overall bolometric luminosity by assuming a fixed ratio of $L_{\text{Bol}} = 10.4L_B$ at all luminosities and redshifts. Fixing this value also allows for direct comparison with Wyithe & Loeb (2003). Finally, the L_{Bol} of the quasar associated with each outflow is simply computed as $L_{\text{Bol}} = E_k \epsilon_k t_d^{-1}$.

We begin by addressing the spatial distribution of quasars, which serves as a check of our merger-based approach. To quantify this distribution, we construct the spatial correlation function of quasars using the center-of-mass information from the outflow data produced in the simulation. In principle, this should be computed accounting for the finite lifetime of each quasar, according to eq. (3). In practice, these times are long enough that such effects can be ignored for distances $\lesssim ct_d \approx 20(1+z)^{-1/2}$ comoving Mpc. Thus we calculate the 3-dimensional real space correlation function using the simplest estimator,

$$\xi_{qq}(z, m)_k + 1 = \frac{DD(z, m)_k}{RR(z, m)_k}, \quad (8)$$

where $DD(z, m)_k$ is the number of pairs with a magnitude greater than some limit, separated by a comoving

difference corresponding to a bin k , and $RR(z, m)_k$ is the average number of pairs that would be found at a given separation in a random distribution of points with an overall density equal to the mean density of observable quasars.

We next adopt a fixed magnitude limit in the B-band of 20.84, to allow for comparisons with observations from the 2dF quasar redshift survey (Croom *et al.* 2001; 2002), which have an overall photometric b band limit of 20.9, where $B \approx b + 0.06$ (Goldschmidt & Miller 1998). This can be computed as

$$B = 5.5 - 2.5 \log_{10} \left(\frac{L_B}{L_\odot} \right) + 5 \log_{10} \left(\frac{d}{10 \text{pc}} \right) + 2.5(1 - \alpha_\nu) \log_{10}(1 + z), \quad (9)$$

where d is the comoving distance to the quasar, and $\alpha_\nu = -0.5$ is the typical slope of the quasar power-law continuum (Wyithe & Loeb 2005).

A detailed examination of short range quasar correlations is given in the Sloan binary quasar study of Henawi *et al.* (2006). To compare to their sample we project the redshift space correlation function within a maximum velocity range of $|\Delta v| < 2000 \text{ km s}^{-1}$, to give

$$w_{qq}(R, z) = \frac{1}{s_{\text{max}} - s_{\text{min}}} \int_{s_{\text{min}}}^{s_{\text{max}}} \xi_{qq}(R, s, z) ds. \quad (10)$$

Here the integration limits are set by $s_{\text{max}} = -s_{\text{min}} = 2000/aH(z)$ corresponding to the width of the velocity interval. Note that in determining $w_{qq}(R, z)$, rather than integrating over the redshift space correlation function we instead use the real space version. This is a good approximation since the defined velocity interval is sufficiently large to contain most of the velocity distribution in the redshift direction.

In Figure 1 we plot the real space correlation function in the $z = 2.0 - 3.0$ and $z = 1.2 - 2.0$ ranges. On scales larger than 1 Mpc the agreement with the Croom *et al.* (2001) results is strong, with our results showing a small excess over the mean observational result. The overlay of the higher redshift results in the middle panel shows, as expected, that the redshift evolution at these early times is very weak. On sub-Mpc scales there is a noticeable turn-up, which is best examined using the projected correlation function $w_{qq}(R, z)$, shown in the bottom panel. To compare to the Croom *et al.* (2001) results we have projected their real space correlation function fit, and also extended this fit below their nominal cutoff. This provides a clear quantitative baseline for

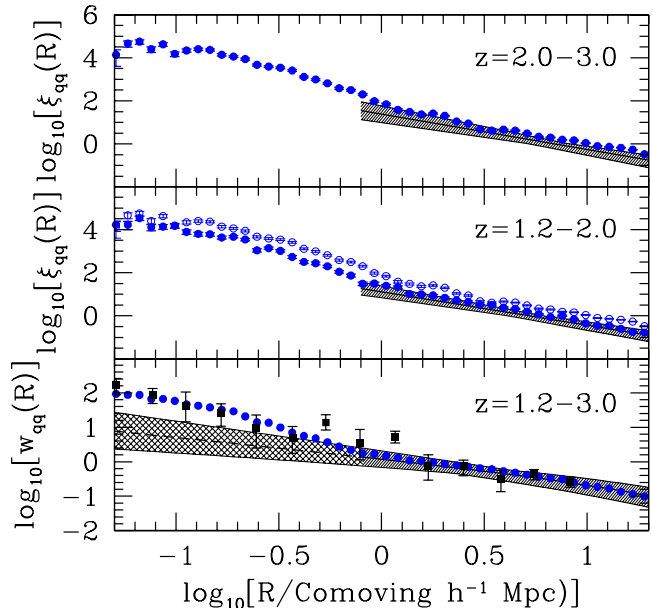


FIG. 1.— *Top*: Real space correlation function of $B < 20.9$ quasars from $z = 2$ to 3. The points are taken from our large 1020 run, while the solid line is the ($2.1 \leq z \leq 2.9$) fit to the 2dF quasar redshift survey by Croom *et al.* (2001), bounded by the measurement errors. Note that this measurement does not extend to separations below 0.8 Mpc h^{-1} . *Center*: Real space $B < 20.9$ quasar correlation function from the 1020 simulation from $z = 1.2$ to 2, as compared with the $1.35 \leq z \leq 1.7$ Croom *et al.* (2001) results. Symbols are as in the upper panel, while the open circles are the simulated $2 \leq z \leq 3$ correlation function, shown for comparison. *Bottom*: Angular correlation function of $B < 20.9$ quasars. The solid circles are taken from the simulation at $z = 1.2 - 3.0$, while the solid line is the Croom *et al.* (2001) observations, projected and averaged over the same redshift range. The cross-hatched region is an extrapolation of the Croom *et al.* (2001) fit to smaller separations, which helps to highlight the excess in w_{qq} at small separations observed by Hennawi *et al.* (2005). This excess is well reproduced in our simulations, where it arises from gravitationally bound pairs of quasars (the so-called “one halo contribution”).

examining the short-scale clustering excess observed by Hennawi *et al.* (2006). The precise position and magnitude of the clustering excess are reproduced extremely well within our simulation, which we take as both support for our approach and validation of the Hennawi *et al.* (2006) results.

This turn up, which has also been observed in the high-redshift Lyman break galaxy population (Ouchi *et al.* 2005) as well as in a local sample of galaxies (Zehavi *et al.* 2004), is most likely due to gravitationally bound pairs of quasars that are orbiting each other. This so-called “one halo” contribution (*e.g.* Bullock *et al.* 2002; van den Bosch *et al.* 2003; Magliocchetti & Porciani 2003) should become important at distances less than

$$d_{1\text{halo}} \approx \left[\frac{m_Q}{(4\pi/3)\Omega_0\rho_c} \right]^{1/3}, \quad (11)$$

where m_Q is the mass of the halos associated with the quasars above our magnitude limit. From the large scale clustering this is $\approx 2 \times 10^{12} M_\odot$, corresponding to the $\approx 1.0 \text{ Mpc}$ position of the turn-up, lending further weight to this interpretation.

3.2. Quasar-Galaxy Cross-Correlation Function

As a complementary investigation, we also examine the cross-correlation function between quasars and galaxies, ξ_{qg} . By cross-correlating these two populations we are directly able to evaluate whether galaxies containing quasars are clustered differently than similar-mass quiescent galaxies. Early observational attempts to measure ξ_{qg} were limited by sample size and thus a bias toward 2-dimensional angular measurements prevailed (*e.g.* Ellingson, Yee & Green 1991; Smith, Boyle & Maddox 1995; Croom & Shanks 1999). However, the SDSS and 2dF quasar surveys have enabled cross correlations in 3-dimensions below a redshift limit of $z < 0.3$ (Croom *et al.* 2003; Wake *et al.* 2004) and a study at intermediate redshifts using the DEEP2 data has been undertaken (Coil *et al.* 2006). To date, these investigations have not uncovered any bias in ξ_{qg} on scales down to the minimum scale to which they are sensitive, which is around 1 Mpc.

To evaluate ξ_{qg} we use the quasar catalog from the previous section, combined with a galaxy catalog evaluated with a FOF group finder on the baryonic material in our simulation. We use a linking length $b = 0.065$ to find groups with an outer density limit of $\delta \simeq 2000$. With a baryonic mass cut of $10^{10.5} M_\odot$ we find 37,995 groups, and for $10^{11} M_\odot$ we find 11,857 groups. The estimator for the cross correlation function is

$$\xi_{qg}(z, m)_k + 1 = \frac{D_q D_g(z, m)_k}{R_q R_g(z, m)_k}, \quad (12)$$

where $D_q D_g(z, m)_k$ is the number of quasar-galaxy pairs above the magnitude limit in bin k , and $R_q R_g(z, m)_k$ is the number of quasar-galaxy pairs that would be expected if these objects were randomly distributed with the same densities as in our simulation.

Our results are plotted in Figure 2, in which we now employ an *absolute* magnitude limit of $M_B = -22$, to better compare with observations. On scales larger than 1 Mpc, ξ_{qg} is indistinguishable from ξ_{gg} , in agreement with observations. This is true regardless of whether we choose the $M_b > 10^{10.5} M_\odot$ or $M_b > 10^{11} M_\odot$ galaxy populations. However, on scales below $600 \text{ h}^{-1} \text{ kpc}$, ξ_{qg} exhibits a clustering *enhancement*. At first glance, this would appear to be consistent with our results from §3.1, which show that one-halo effects can create an excess of clustering at small scales. However, the explanation cannot be this straightforward. In the bottom panel of Figure 2 we plot the ratio ξ_{qg}/ξ_{gg} , which shows explicitly the turn-over from large-scale agreement to short-scale excess. At large separations, active galaxies are clustered very similarly to the general population, consistent with the DEEP2 results. Yet at small separations, a dramatic change occurs. Despite the fact that the one-halo contribution is implicitly included in ξ_{qg} , *the amplitude of the break in the cross correlation function exceeds that of the galaxy autocorrelation function by a factor of ≈ 2.5 .*

Thus it appears that our identification of quasars with mergers enhances their clustering on the smallest scales. At first it seems that this is strongly at odds with previous theoretical studies of mergers (Percival *et al.* 2003; Scannapieco & Thacker 2003). However, these studies were targeted to separations larger than 1 Mpc, where the two-halo term is the dominant contribution to the correlation function. The excess we find here occurs

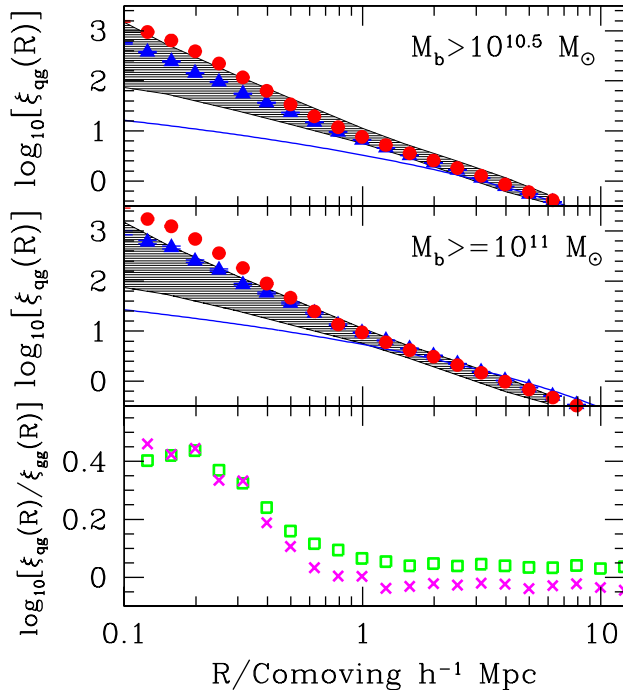


FIG. 2.— *Top*: Real space cross-correlation function, ξ_{qg} , of $M_B \lesssim -22$ quasars to galaxies with baryonic masses above $10^{10.5} M_\odot$ (circles) as compared to the autocorrelation function of these galaxies (squares). The selected mass and magnitude limits have been chosen to be in broad agreement with the quasars and galaxies used in measuring the cross-correlation function from the DEEP2 survey (Coil *et al.* 2006). These observations are shown as the shaded region, which is an estimate that adopts the errors from the projected cross-correlation function, around the best fit to the spatial correlation function, $\xi_{qg}(r) = (r/3.45)^{-1.68}$. Finally the solid lines gives the linear correlation function of $10^{12} M_\odot$ halos. *Center*: Real space quasar-galaxy cross-correlation function and galaxy-galaxy correlation function, but now associating galaxies with objects with baryonic masses above $10^{11} M_\odot$. Symbols are as in the upper panel. *Bottom*: Ratio of quasar-galaxy cross-correlation function to galaxy-galaxy correlation function in the $M_b \geq 10^{10.5} M_\odot$ case (squares) and $M_b \geq 10^{11} M_\odot$ case (crosses). The cross correlation function not only exhibits a break below 1 comoving Mpc h^{-1} , but this break is stronger than in the galaxy-galaxy autocorrelation function. The strengthening of this break is related to the merger nature of quasars in our simulation, and is consistent with local measurements (Serber *et al.* 2006), but unfortunately occurs at too small scales to be measured at $z \approx 1$ from current surveys.

purely in the one-halo regime, meaning that mergers have an excess of very close neighbors.

In support of our results, local studies of quasar-galaxy clustering have found an excess of galaxies at radii < 0.5 Mpc, completely analogous to the one in our simulation. Studying a $z < 0.3$ sample of quasars drawn from the Sloan Digital Sky Survey (SDSS), Serber *et al.* (2006), have found that $M_i < -23.3$ quasars are more than three times more clustered than L^* galaxies on $\lesssim 0.1$ Mpc h^{-1} scales, although they cluster similarly to L^* galaxies on larger scales. While this study was carried out at much lower redshift, these quasars have roughly the same intrinsic magnitudes as those in Figure 2, as can be estimated assuming a typical redshift of $z \approx 1.4$, which for our simulated sample gives a distance modulus

of ≈ 45 or $M_B \lesssim -24$. Thus there seems to be mounting observational and theoretical evidence that the correlation function of the products of mergers, while only very weakly enhanced at large separations, may nevertheless be more strongly enhanced in the one-halo regime.

In fact, an intriguing possibility is that this is caused by three-body interactions in which a third galaxy removes angular momentum from a nearby close pair. This suggests that dynamical friction may not always be the dominant process driving galaxy mergers. Rather, a significant number may be caused by a process more akin to the formation of tight binaries in dense star clusters (*e.g.* Rasio, Pfahl & Rappaport 2000). Clearly this issue merits future investigation.

3.3. Optical Quasar Luminosity Function

To construct the luminosity function for each luminosity and redshift bin, we calculate the number of quasars in this bin times the total time these objects are shining, and divide by the time interval, the width of the bin, and the volume of the simulation. That is for a given redshift bin i and a given luminosity bin j the luminosity function is simply

$$\Psi_{i,j} = \frac{1}{V \Delta t_i \Delta L_{B,j}} \sum_{k \in \text{bin}_{i,j}} t_{d,k}, \quad (13)$$

where the sum is over all quasars with redshifts and luminosities associated with the i, j bin, which spans a time interval Δt_i and a range of luminosities $\Delta L_{B,j}$. In Figure 3 we plot the resulting luminosity function for our fiducial 1020 simulation.

The dotted line in this plot gives the Wyithe & Loeb (2003) estimate of the luminosity function, which is simply based on a merger prescription and does not account for feedback. Comparing this estimate with our simulation results uncovers a clear turn-down in the number of $L_B \geq 10^{13} L_\odot$ quasars at $z \lesssim 2$. However, comparing the simulation results with the measured points make it immediately clear that this turn down is not as strong as seen in the observations. This means that the suppression is much weaker in the simulation than in the semi-analytic SO4 model, which was found to be a good fit to the observations. This is a surprising result which needs to be understood in more detail, and, to explore this further, we recalculate the luminosity function but imposing by hand the precise gas heating methodology used in the semi-analytic approach.

As emphasized in Oh & Benson (2003) the ability of gas to cool is insightfully described from the perspective of entropy. Under the frequently used definition of entropy, $S = T/n^{2/3}$, the isobaric cooling time may be written,

$$t_{\text{cool}} = \frac{3/2 n k_B T}{n_e^2 \Lambda(T)} = S^{3/2} \left(\frac{3 \mu_e^2 k_B}{2 \mu^2 T^{1/2} \Lambda(T)} \right) = S^{3/2} F(T), \quad (14)$$

where $\mu = 0.62$, $\mu_e = 1.18$, and $F(T)$ serves as temperature dependent normalization. By equating the cooling time to the Hubble time, t_H , we can derive a critical entropy value: gas above this entropy limit is unable to cool within the Hubble time and is thus effectively removed from the galaxy formation process. The critical value is

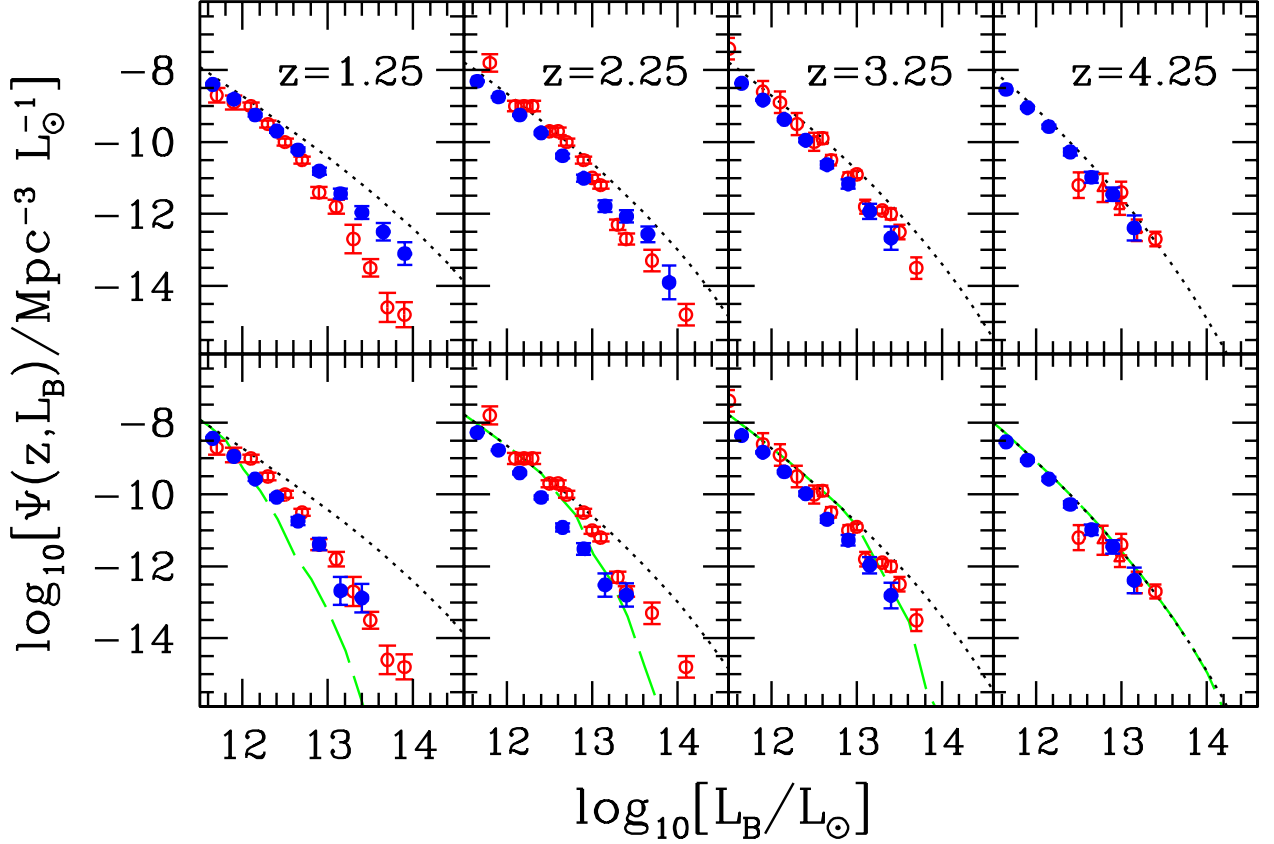


FIG. 3.— Evolution of the B-band quasar luminosity function. Here the data points are taken from Pei (1995, open circles), which are derived from the compilation by Hartwick & Schade (1990), and Fan (2001, open triangles). Simulation results are given by the solid points, while the dotted line is the simple estimate from the analytic model by Wyithe & Loeb (2003), which does not include feedback. From left to right the columns give results at redshifts of 1.2-1.75, 1.75-2.75, 2.75-3.75, and 3.75-4.75 respectively. The top row shows the raw simulation results, while the bottom row shows the luminosity function derived by applying the same physical model as SO04 to the simulation quasar catalog, along with the fiducial SO04 model with a 5% outflow efficiency (dashed line). The difference at low redshift between the two models arises because the semi-analytic model treats heating and cooling in a significantly different way to the simulation.

(SO04),

$$S_{\text{crit}} = (280 \text{ keV cm}^2)(1+z)^{-1} \left[\frac{E(z)}{(1+z)^{3/2}} \right]^{2/3} \times \left[\frac{\Lambda(T_{\text{min}})}{6.3 \times 10^{-22} \text{ ergs s}^{-1} \text{ cm}^3} \right], \quad (15)$$

where $\Lambda(T_{\text{min}})$ corresponds to the minimum cooling time below 10^8 K ($T_{\text{min}} \simeq 2.3 \times 10^5$ K), and $E(z) = [\Omega_m(1+z)^3 + \Omega_\Lambda]^{1/2}$.

Having defined the concept of critical entropy, we first estimate the total amount of mass that can be heated above S_{crit} using eq. (17) of SO04,

$$M_{\text{ex}}(\delta, z, M_{\text{bh}}) = 4.6 \times 10^{12} M_\odot S_{100, \text{crit}}(z)^{-1} \times E_{60} \delta_s^{-2/3} (1+z)^{-2}. \quad (16)$$

We then search to a radius $R = \min(R_s, R_{\text{heat}})$, where R_s is the shell radius versus time given by,

$$R_s = 1.7 \text{ Mpc } E_{60}^{1/5} \delta_s^{-1/5} (1+z)^{-3/5} t_{\text{Gyr}}^{2/5}, \quad (17)$$

and R_{heat} is the radius of the region heated above S_{crit} as calculated in the SO04 model

$$R_{\text{heat}} = 5.6 \text{ Mpc } S_{100, \text{crit}}(z)^{-1/3} E_{60}^{1/3} \delta_s^{-5/9} (1+z)^{-5/3}. \quad (18)$$

Our assumed S_{crit} is 60 keV cm^2 , corresponding to the metallicity value of $Z = 0.05$ used in our simulation, and we taken an average post-shock overdensity, δ_s , of 20. If a quasar is found within R , we subtract M_{ex} from the gas mass associated with it, and if M_{ex} exceeds this mass, we remove it from our catalog altogether.

The resulting luminosity function is plotted in the second row of Figure 3. In this case, there is significantly better agreement between the data (and the semi-analytic model) for this revised luminosity function. While this model does not precisely reproduce the strong knee observed in the SO04 model and the magnitude of the turn-down at higher luminosities, the improved agreement is compelling. It is thus clear that the primary cause of the difference between these models, is not their varying approaches to modeling quasars themselves, but rather in the simplified exclusion conditions as described by eqs. (16) - (18).

While these equations capture most of the salient features of shock heating, there are two major effects that they fail to address. Firstly, they do not differentiate between material within galaxies and material in the intergalactic medium, while in our simulation we do not apply the outflow heating to the host galaxy itself. Sec-

only, eqs. (16) - (18) assign a single density to all the gas associated with an object that is overtaken by an outflow, whereas heating processes in the simulation are directly affected by the detailed substructure in this gas.

To explore the relative impact of these two effects, we examine the distribution of progenitor halo labels in the three largest outflows in our simulation at an epoch of $z = 1.3$. These systems have baryonic masses ranging from $4.7 \times 10^{12} M_{\odot}$ to $5.1 \times 10^{12} M_{\odot}$, and the majority of particles within them have a single label associated with the previous outflow event. To determine the number of particles with dissimilar labels we place a sphere at the center of mass of the group and then fit a radius (by hand) to enclose the outer boundary of the particles with the main group label. The typical radius of this outer boundary was 250 kpc. For all systems we found a significant amount of substructure as evidenced by all groups having at least 18, and typically more than 40, distinct labels each with at least 20 particles. The total number of particles with labels distinct from the main group was always close to the merger mass limit, indicative of a system just about to undergo the outflow event associated with the merger.

This results seems to suggest that both effects may be contributing to the reduced suppression, as each outflow is associated with a large group with a single index (that might have been disrupted if in-galaxy heating was included), which merges with a collection of remnants with many indices (that might not have been accreted if in-shock heating were more efficient). Ultimately, the stronger agreement for the revised catalog versus that of the original simulation indicates that both of these issues need to be explored further. On the simulation side this would involve contrasting the present results with a model that includes more efficient ejection of gas from galaxies themselves. Likewise, in the semi-analytics the efficiency of heating could be parameterized by adding an additional parameter to account for in-shock cooling, although it would be necessary to conduct detailed simulations of this process to precisely calibrate this number. These are significant issues which we will return to in the discussion.

Finally, as a test of convergence, in Figure 4 we compare the luminosity function in our fiducial simulation with that derived from our $35 h^{-1} \text{Mpc}^3$ simulations. In this case we do not impose eqs. (16) - (18). At all redshifts we obtain good agreement between runs over the luminosity range spanned by these smaller simulations volumes, although the 400 results are very noisy. Note that while in the $z \approx 2.25$ column, the luminosity function in the 3200 run has fewer large quasars than the other runs, this is due to small number statistics and the fact that it was stopped earlier than the other simulations due to the excessively large number of time-steps required. Similarly, $L_B \geq 10^{13} L_{\odot}$ quasars are so rare that they can not be compared between the 1020 simulation and the test simulations, motivating our choice of an extremely large volume for this run.

3.4. Hard X-ray AGN Luminosity Function

Our simulation can also be directly compared with observations of the hard X-ray luminosity function, which we construct from our bolometric luminosities using a similar approach to that for the optical quasar luminosity

function. To convert from the bolometric luminosity to L_X we use results from Marconi *et al.* (2004) who calculated the expected correction for $\approx 10^{12} L_{\odot}$ AGN with a spectral template motivated by recent observations. The ratio of the bolometric luminosity to the hard X-ray band (2-10 keV) is given by a third-degree polynomial,

$$\log[L/L(2-10 \text{ keV})] = 1.54 + 0.24\mathcal{L} + 0.012\mathcal{L}^2 + 0.0015\mathcal{L}^3, \quad (19)$$

where $\mathcal{L} = \log(L_{\text{Bol}}) - 12$, and L_{Bol} is given in L_{\odot} .

Early observational work used ASCA data (Boyle *et al.* 1998) and BeppoSax data (La Franca *et al.* 2002) to show that the hard X-ray luminosity function (HXLf) was evolving strongly between $z = 0$ and 1.5, consistent with pure luminosity evolution. More recently, Cowie *et al.* (2003) used *Chandra* data in two redshift bins ($z=0.1-1$ and $z=2-4$) to argue that the AGN number density for luminosities lower than $10^{44} \text{ erg s}^{-1}$ seems to peak at a lower redshift than those of higher luminosity. This anti-hierarchical evolution was demonstrated definitively by Ueda *et al.* (2003), who carried out a comprehensive compilation of HEAO1 (Piccinotti *et al.* 1982; Grossan 1992), ASCA (Ueda 2001, Akiyama *et al.* 2003) and *Chandra* (Brandt *et al.* 2001) data to derive the comoving spatial density of AGNs in three luminosity ranges between $\log(L_X) = 41.5$ and $\log(L_X) = 48$.

In Figure 5 we compare our derived spatial densities to the observational data in the $\log(L_X) = 43 - 44.5$ and $\log(L_X) = 44.5 - 48$ luminosity bands in this sample. Both the qualitative and quantitative predictions of the simulation agree with the measurements: the downsizing trend is apparent in both luminosity bands and the overall normalizations agree well. However, below $z \simeq 2$, we are faced with two minor issues. Firstly, in the lower luminosity bin it appears that the luminosity function is turning down slightly too quickly, as the observations suggest that the turn down in this luminosity range occurs after $z = 1$. Secondly, the brightest band, while turning down at the observed epoch of $z = 2$, does not perfectly follow the observational trend. Imposing the exclusion conditions represented by eqs. (16) - (18) improves this fit somewhat, although these differences are small compared to the measurement errors from the observations. Imposing these conditions has no impact on the lower luminosity bin. In general, these results are consistent with those in §3.3.

4. OTHER IMPLICATIONS

4.1. Impact on the Intergalactic Medium

While our study has been focused on the properties of the quasar population itself, our simulations naturally have predictions for the more tenuous gas surrounding large galaxies. In fact, as discussed above, the most clear observational evidence for widespread nongravitational heating lies not in the galaxy population, but rather in the properties of the diffuse gas in galaxy clusters.

To examine the impact of outflows on this material we first focus on the total amount of gas that has been shocked to $S > S_{\text{crit}}$, such that it no longer participates in fueling further generations of quasars. The redshift evolution of the mass fraction of this gas is plotted in the upper panel of Figure 6, which shows that quasar feedback is primarily a low-redshift phenomenon. Thus, above $z \approx 3$ less than 3% of the gas in the simulation has

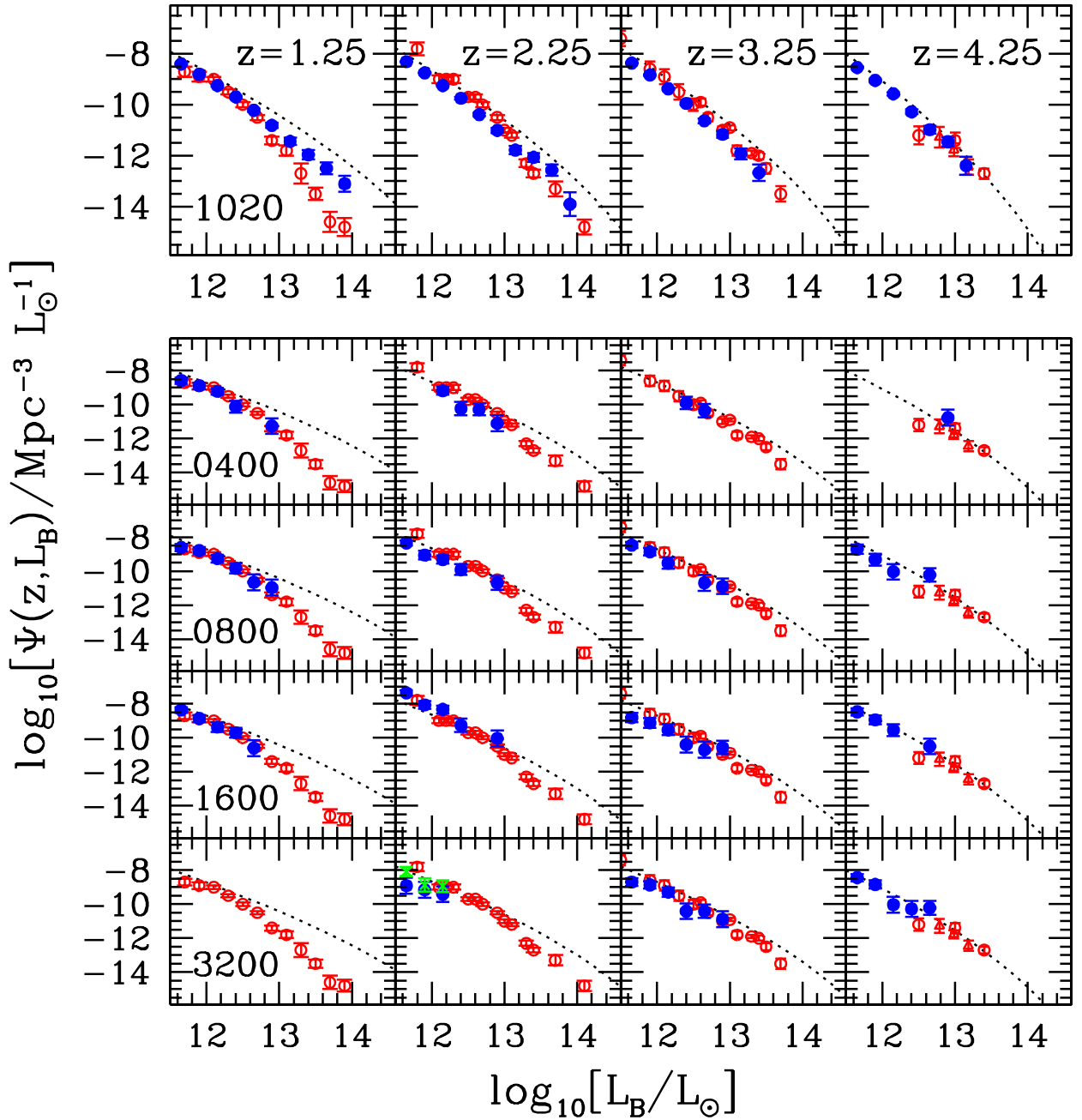


FIG. 4.— Evolution of the B-band quasar luminosity function as a function of resolution. Again the data points are taken from Pei (1995, open circles) and Fan (2001, open triangles), as compiled by Hartwick & Schade (1990). Simulation results are given by the solid points, while the dotted line is the simple estimate from the analytic model by Wyithe & Loeb (2003), which does not include feedback. From left to right the columns give results at redshifts of 1.0-1.75 (1.2 – 1.75 in run 1020), 1.75-2.75 (2.5-2.75 in run 3200), 2.75-3.75, and 3.75-4.75 respectively. From top to bottom, the rows show results from our large ($146h^{-1} \text{ Mpc}^3$) run 1020, and the smaller ($35h^{-1} \text{ Mpc}^3$) runs 0400, 0800, 1600, and 3200. Symbols are as in Figure 3, and, for comparison, the crosses in $z = 2.5 - 2.75$ panel of the 3200 run show the results of the 1600 run limited to this same redshift range.

been affected, consistent with the lack of suppression of the luminosity function at these redshifts. At lower redshifts, however, the $S > S_{\text{crit}}$ mass fraction grows prodigiously, preventing roughly 20% of the gas in the simulation from cooling. This is consistent with the turn-down

in the luminosity function seen in Figure 3, which while not as efficiently quenched as the semi-analytic results, nevertheless differs substantially from the pure-merger predictions.

As a test of convergence, we also plot in this panel the

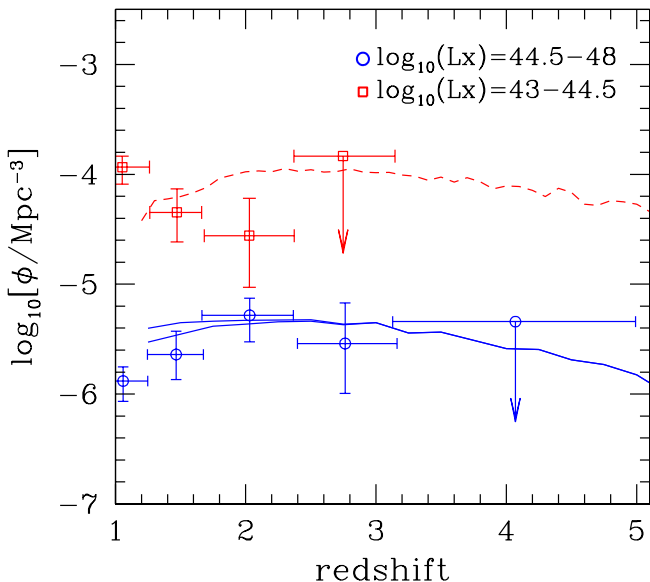


FIG. 5.— Hard X-ray luminosity function. The solid and dashed lines give the number density of X-ray luminous ($44.5 \leq \log_{10}(L_X) \leq 48$) and X-ray faint ($43 \leq \log_{10}(L_X) \leq 44.5$) AGN in our 1020 simulation, respectively. In the luminous case, the lower solid curve shows the results in which the exclusion conditions, eqs. (16) - (18) are imposed. These models are compared with observations of luminous (circles) and faint (squares) AGN as compiled by Ueda *et al.* (2003).

$S > S_{\text{crit}}$ mass fraction from each of our smaller simulations. These range from the 0400 run, in which particles are 64 times more massive than in the 1020 simulation, to the 1600 run, in which particles are 0.125 times the mass of those in the 1020 run. As increasing resolution adds a large number of low-mass, high-redshift outflows, the mass fractions at high redshift increase monotonically with resolution. At lower redshift, however, the mass fractions approach each other asymptotically, and in the important $z \lesssim 3$ range, this quantity is largely consistent across runs. However, this mass convergence does not give a complete picture of the effect of resolution.

In the lower panel of Figure 6 we plot the evolution of the volume filling factor of $S \geq S_{\text{crit}}$ gas in each of these runs. To calculate these quantities in the SPH method it is necessary to first smooth the particle data on to a grid. In the 1020 case we do so on a 1340^3 mesh, so that the smoothing scale for the filling factor at expansion factor a is $0.155a$ Mpc, which is considerably above our minimum smoothing length. In the other runs we use a mesh of size twice the particle resolution, for example, the 2×160^3 run was smoothed on to a 320^3 mesh.

The data point in this panel gives the upper limit on the volume filling factor provided by the Lyman- α forest (Levine & Gnedin 2005), which is well above our results, as expected from the semi-analytic estimates in SO04. For comparison, we also plot the results from a range of models taken from the N-body + semianalytic study of Levine & Gnedin (2005). While this is substantially higher than our results, this is to some degree due to the fact that they computed the full volume impacted

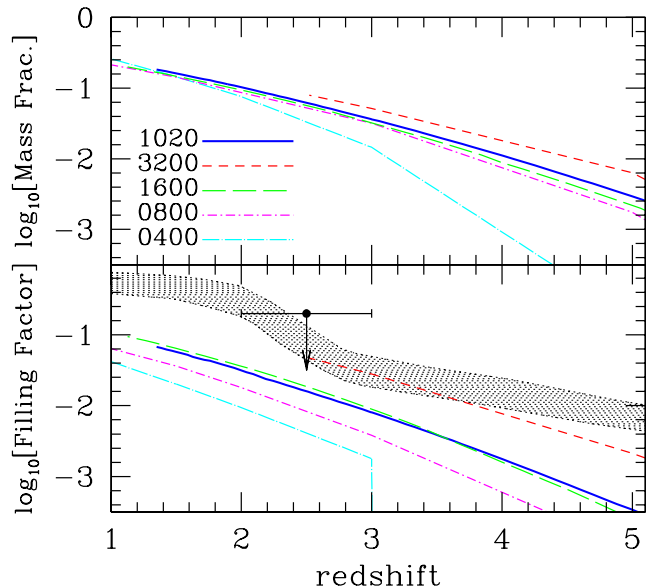


FIG. 6.— *Top*: Mass fraction of gas heated above S_{crit} as a function of redshift. The solid line shows the results from our large 1020 run, while the short dashed, long dashed, dot short-dashed, and dot long-dashed, lines (which move from higher to lower filling factors) show the results of our 3200, 1600, 0800, and 0400 runs, respectively. *Bottom*: Volume filling factor of gas heated above S_{crit} as a function of redshift. Lines are as in the upper panel, while the point gives the Ly α forest constraint discussed in Levine & Gnedin (2005, see also Davé *et al.* 1999). Finally, the shaded region gives the estimate of the volume filling factor impacted by AGN outflows in Levine and Gnedin (2005), and is bounded from below by their $\epsilon_k = 0.05$, $\tau_{\text{AGN}} = 10^7$ yr model and bounded from above by their $\epsilon_k = 0.05$, $\tau_{\text{AGN}} = 10^8$ yr model.

by quasars outflows, rather than only the volume heated above S_{crit} .

Furthermore, it is clear from this figure that the volume filling factors are significantly different across simulations, even at the lowest redshifts. This result seems at odds with our mass-fraction measurements. To explore this issue further, in Figure 7 we choose a fixed redshift of $z = 3$ and plot the mass fraction and volume filling fraction above a threshold entropy S_{thresh} , which we allow to vary. For all three models, the mass fraction is only a weak function of S_{thresh} for all entropy values near S_{crit} . This means that small differences in entropy have only a small impact on the number of particles prevented from cooling, and therefore both the $S > S_{\text{crit}}$ mass fraction (shown in Figure 6) and the luminosity function (shown in Figure 4) are similar across runs. Essentially, at $z = 3$, the particles are divided into two types, those whose entropies are well above S_{crit} , and those that are far below this critical value.

In the lower panel of Figure 4, we plot the volume filling factor as a function of S_{thresh} , again at $z = 3$. In this case, near S_{crit} the volume filling factor is a strong function of our threshold entropy. This suggests that the high entropy gas is largely found in low density environments, so that changes in S around S_{crit} pass through a region where the volume can change rapidly, but there is actually little mass to modify the overall mass fraction.

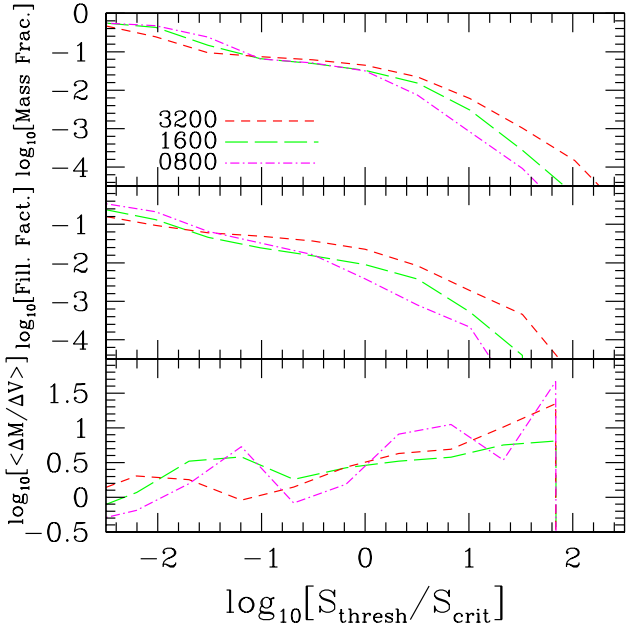


FIG. 7.— *Top*: Mass fraction of gas heated above a given entropy threshold, S_{thresh} in or 3200 (short-dashed), 1600 (long-dashed), and 0800 (dot-dashed) simulations, at a fixed redshift of $z = 3$. *Center*: Volume filling factor above a given threshold at $z = 3$. Lines as in the upper panel. For our choice of metallicity, $S_{\text{crit}}(z = 3) = 19 \text{ keV cm}^2$, and near this critical value, the volume filling factor is a strong function of the threshold entropy, but the mass fraction is almost constant. *Bottom*: Average differential overdensity (change in mass fraction over change in volume filling factor) as a function of S_{thresh} .

In the lower panel of Figure 4 we plot the the differential overdensity, $\Delta M/\Delta V$, that is the change in the mass fraction over the change in the volume filling factor, as a function of S . This confirms that the majority of $S \approx S_{\text{crit}}$ gas is in environments only a few times denser than the mean, and that the density of this material is increasing strongly as a function of entropy.

Figure 8 illustrates why this is this case. Here we show the entropy distribution in slices taken from our 1020 simulation at the final output redshift. It is clear from this plot that the boundary between $S > S_{\text{crit}}$ and subcritical gas (indicated by the white lines) lies at the very edges of cosmological halos, where the density is dropping off strongly. These boundaries are defined by comparatively few SPH particles, and thus their positions can change rapidly following small changes in the particle distribution. Finally, the thin slice shown in the smallest-scale panel in Figure 8 uncovers the presence of $S \leq S_{\text{crit}}$ subclumps within a larger (high entropy) region. Again, the presence of this cooling substructure was not included in the SO04 models, and is one of the key causes of the differences between these semi-analytical results and those presented here.

4.2. Impact on Clusters and Groups

Recent *Chandra* observations of Hydra A (Nulsen et al 2005) have uncovered evidence for AGN activity within clusters at intermediate redshifts. While cooling flow clusters at lower redshift seem inconsistent with the idea

of powerful shocks (*e.g.* Voit & Donahue 2005, Croton *et al.* 2006), it remains an intriguing possibility that these systems underwent an earlier period of strong feedback and have now settled into a quiescent state. The observations of radio quiet clusters by Donahue *et al.* (2005) that show extremely long cooling times despite an absence of inferred black hole activity, are broadly consistent with this hypothesis. These results prompted the numerical investigations of Sijacki & Springel (2006) who showed that their model of AGN activity has comparatively little effect on the cluster $L_X - T$ relationship when all material within the virial radius is included. Therefore in this section we examine the effect of our outflow model on the $L_X - T$ relationship and the cluster entropy profile. It is worth noting that as our raw luminosity function shows we have an excess of bright quasars at $z=1.25$, the results we derive in this section are an upper bound on the effect of outflows on clusters.

To find cluster groups we first begin from a friends-of-friends $b=0.2$ catalogue of the 1020 simulation. The centers of mass are evaluated for these groups, and then used as the beginning stage of an iterative spherical-overdensity group finder that searches radially outward until the group is below the density threshold. The center of mass is then evaluated and used as the beginning point for the radial search, with the process being repeated five times. This technique has the advantage of biasing against mergers since the center of mass of mergers is usually sufficiently offset from the merging groups to stop the spherical-overdensity convergence process early, and the group is then discarded due to the low amount of mass found. We find 1272 groups by this process.

To estimate the bolometric luminosity of the simulated clusters we use

$$L_{\text{Bol}} = \sum_{i=1}^{N_{\text{group}}} \frac{m_i \rho_i}{(\mu m_p)^2} \Lambda(T_i), \quad (20)$$

and the emission weighted temperature is given by,

$$T_{ew} = \frac{\sum_i m_i \rho_i \Lambda(T_i) T_i}{\sum_i m_i \rho_i \Lambda(T_i)}. \quad (21)$$

In these formulae, $\Lambda(T_i)$ is the pure bremsstrahlung estimator of Pearce *et al.* (2000) (see also Navarro *et al.* 1995 and Muanwong *et al.* 2001, for similar approaches), and m_i, ρ_i, T_i are the mass, density and temperature of particle i . While we could use the emission curve associated with the $Z = 0.05$ metallicity gas used in the simulation, the strong peak caused by collisional excitation of He^+ at 10^5 K will give a very high weighting to the cores of clusters, which in fact would probably have cooled significantly if we were using a $Z = 0.3$ metallicity gas. Overall, as emphasized in Muanwong *et al.* (2001), our choice of a pure bremsstrahlung estimator will bias our luminosities low.

Under the assumption of self-similar evolution for spherically symmetric clusters, and also that bremsstrahlung emission dominates in the X-ray band, the luminosity-temperature relationship scales with redshift according to (Kaiser 1986, Maughan *et al.* 2006),

$$E(z)^{-1} \Delta(z)^{-1/2} L \propto k T^2 f_g, \quad (22)$$

where $E(z)$ is the cosmological evolution factor, Δ corresponds to the virial overdensity at a given redshift (*e.g.*

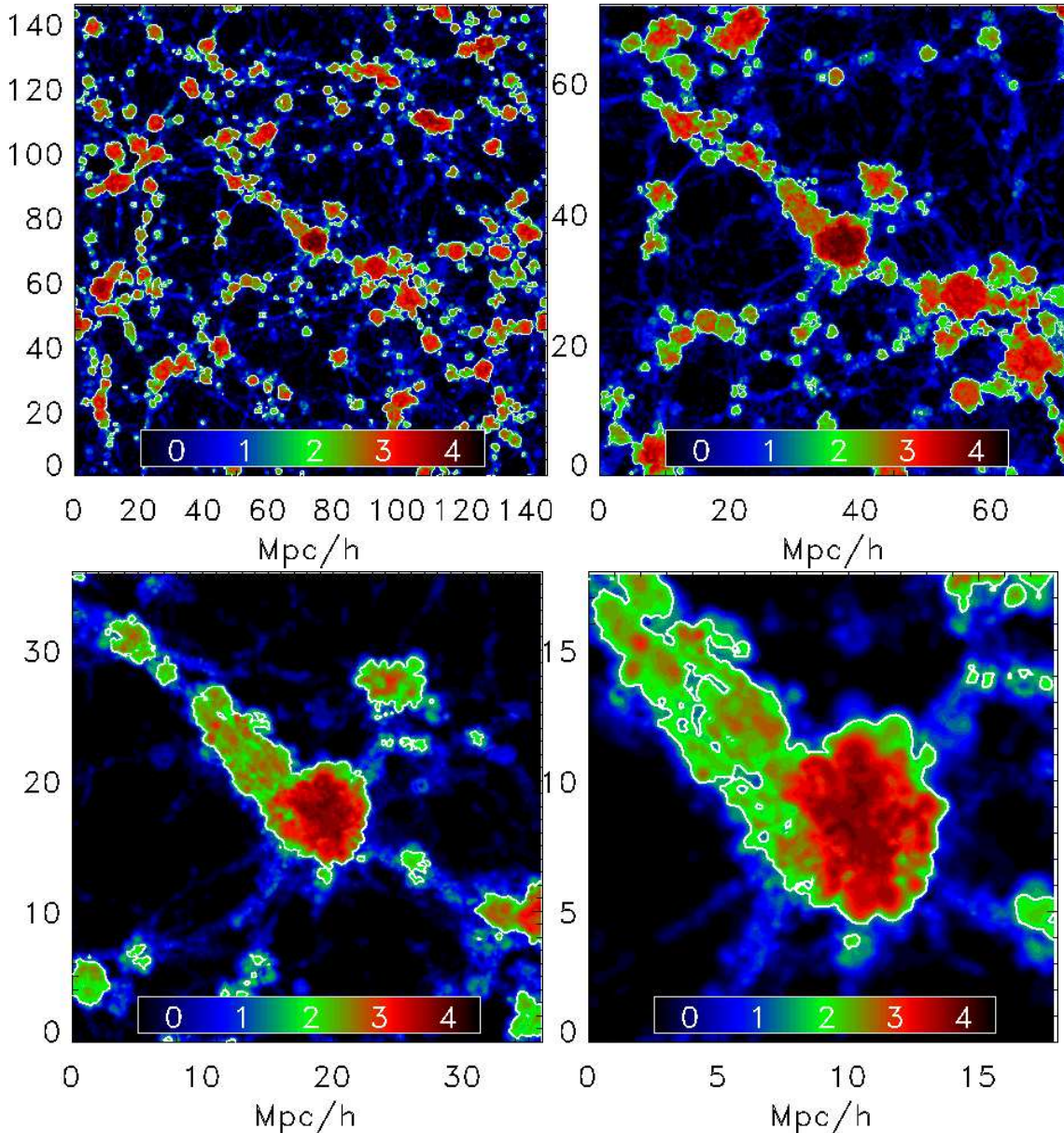


FIG. 8.— *Top*: Contours of entropy from $z = 1.2$ slices through in our 1020 simulation. In the upper two panels the thickness of the slice is $2.4 \text{ Mpc } h^{-1}$, while, to emphasize substructure, the thickness in the $36 \text{ Mpc } h^{-1}$ and $18 \text{ Mpc } h^{-1}$ panels is taken to be $1.2 \text{ Mpc } h^{-1}$ and $0.6 \text{ Mpc } h^{-1}$, respectively. All units are comoving. In each panel the white lines demarcate the boundary at which $S = S_{\text{crit}}$. In general, this occurs at the very edge of halos, where the density is dropping rapidly, but it also occurs in isolated subclumps in otherwise $S \geq S_{\text{crit}}$ regions.

see Bryan & Norman 1998) and f_g is the cluster gas fraction (which is assumed to be independent of z and kT following observations of high redshift clusters, *e.g.* Allen *et al.* 2002). Thus the redshift evolution in the $L_X - T$ relationship can be scaled by dividing the luminosity by $E(z)(\Delta(z)/\Delta(0))^{-1/2}$. While we could thus scale the $L_X - T$ relationship for $z = 0$ clusters back to our final redshift, a recent analysis by Maughan *et al.* (2006) of the WARPS clusters in the region $0.6 < z < 1.0$, provides an unscaled $L_X - T$ relationship at $z \approx 1$. Thus in what follows we use their results as a comparison. We also note that there are no observations of galaxy groups at these epochs.

We plot our results for the $L_X - T$ relationship in Fig-

ure 9, and also show the fit of Maughan *et al.* (2006). It is immediately noticeable that our raw data show a very large scatter in luminosities. Since the luminosity of clusters is linearly weighted by the density, we decided to plot radial profiles of our clusters to determine whether any “overcooling” effects (*e.g.* Thacker *et al.* 2000) might be present (see figure 11). The radial profile shows that the most massive clusters do indeed show a sudden upturn in density in their cores along the lines observed in test problems. We therefore applied a density-cut (filter) at $\delta < 5 \times 10^4$ to the gas in our clusters, which cuts out this problem region. The resulting data is plotted in the right hand panel of figure 9, and shows a much smaller scatter. A least squares fit for our 1 keV and brighter

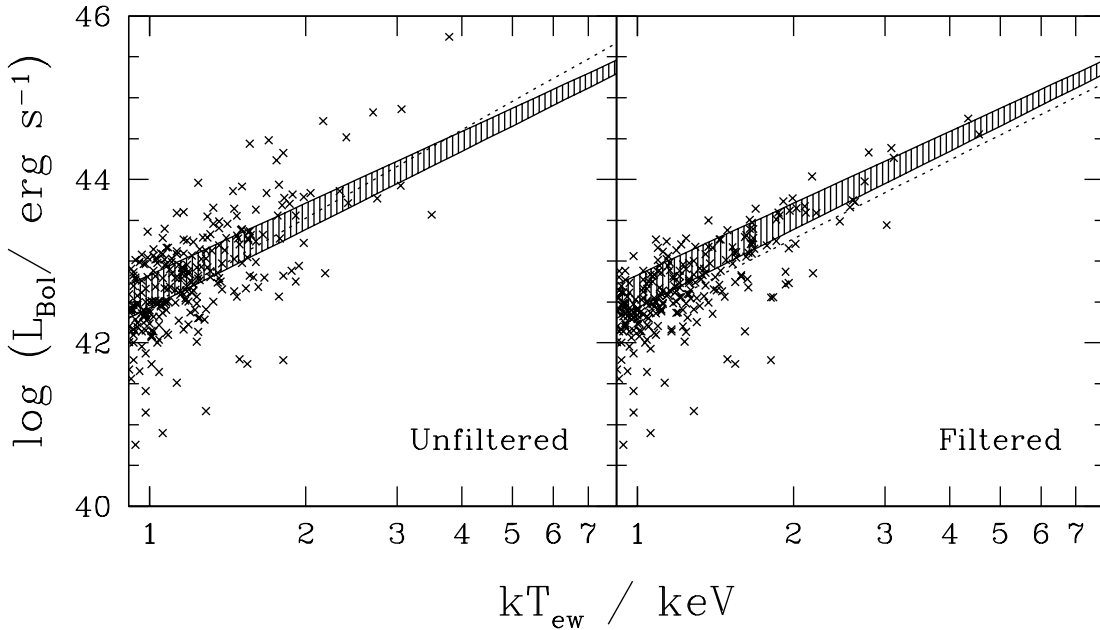


FIG. 9.— $L_X - T$ relationship for the simulated clusters. On the left is the raw unfiltered data including the overly bright core regions (with overdensities exceeding 5×10^4), while the right panel is the filtered data with these regions removed. Dotted lines correspond to least squares fits for clusters above 1 keV. The shaded area corresponds to Maughan *et al.* (2006) fit to the WARPS sample, with the upper limit set by taking the maximum normalization, and the lower limit by matching the exponent of our best-fit to the filtered data.

unfiltered cluster catalogue gives

$$L_{\text{Bol}} = 2.82 \times 10^{42} \left(\frac{T_{\text{ew}}}{\text{keV}} \right)^{3.58}, \quad (23)$$

while the filtered catalogue gives,

$$L_{\text{Bol}} = 2.09 \times 10^{42} \left(\frac{T_{\text{ew}}}{\text{keV}} \right)^{3.18}, \quad (24)$$

which is closer to, albeit slightly less luminous than, the Maughan *et al.* (2006) best fit of $5.4 \times 10^{42} (T_{\text{ew}}/\text{keV})^{2.92}$. Overall, these results are strongly supportive of the conclusions of Sijacki & Springel (2006).

Lower redshift observations of groups (*e.g.* Xue & Wu 2000), show the power law exponent for groups is close to 5. For systems below 1 keV (regardless of whether or not they are core filtered) we do not observe any steepening of the $L_X - T$ relationship, and there is evidence of the relationship becoming shallower, indicative of the gas in this systems being quite strongly perturbed. Thus, rather than analyzing relaxed systems, we are in fact analyzing groups that are radiating significantly due to the presence of an outgoing shock. In the event that this shock is sufficient to heat gas above S_{crit} , we might well expect, in the absence of significant further accretion and AGN activity, that these groups expand and cool before $z = 0$. To quantify this hypothesis, we plot the cluster and core entropy versus temperature in Figure 10. Our results are in broad agreement with the analysis of nearby clusters (Ponman *et al.* 2003, Finoguenov *et al.* 2005), and do indeed show that groups tend to show an excess of entropy in their cores. Therefore, we tentatively suggest that the X-ray emission of galaxy groups at $z > 1$ may well be a “smoking gun” for the AGN heating hypothesis.

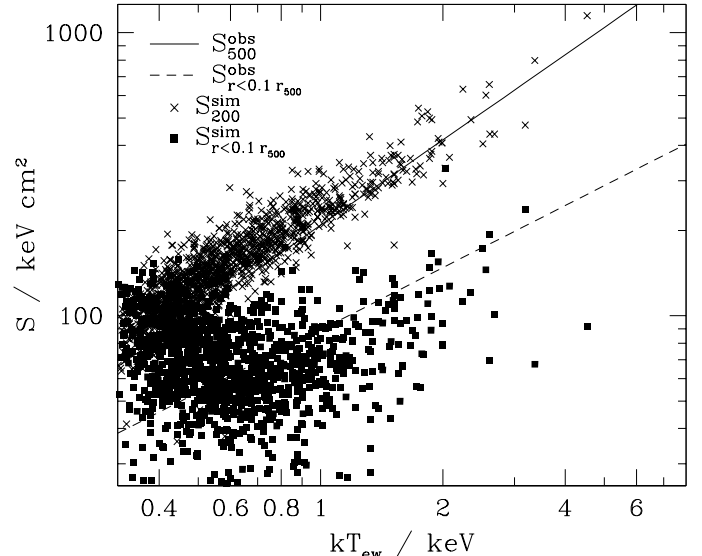


FIG. 10.— Entropy versus emission weighted temperature for different radial cuts. The 4-pointed crosses correspond to the entropy within the virial radius and are compared to the ($z \approx 0$) self-similar ($S \propto T$) fit of Ponman *et al.* (2003) for the entropy within the δ_{500} region, with the normalization taken to match the eight hottest clusters in their sample. The solid squares denote the entropy within $0.1 r_{200}$, a measure of the cluster core entropy. The dashed line is the Finoguenov *et al.* (2005) weighted orthogonal regression fit to the Ponman *et al.* (2003) results. Our results show a significant turn-up in the core entropy at groups scales (< 1 keV).

As well as the radial density profiles, we also show the temperature and entropy profiles in Figure 11. The only

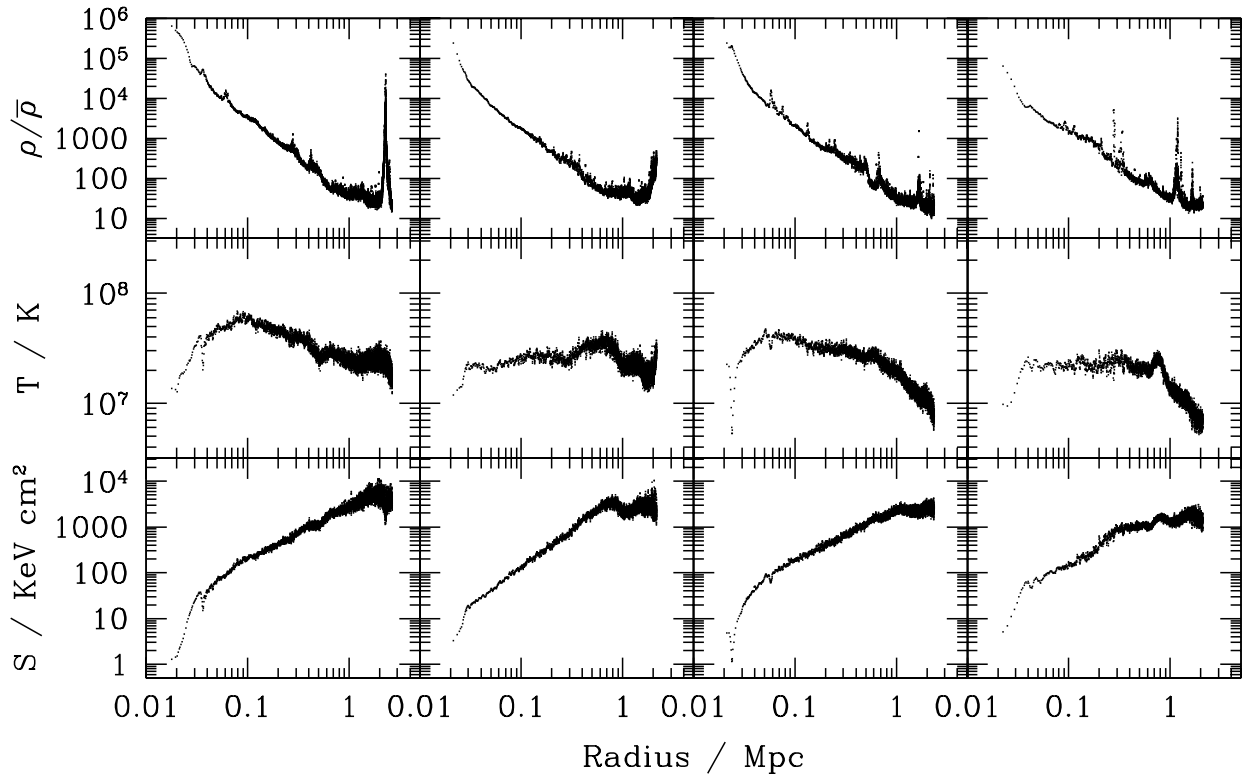


FIG. 11.— Density, temperature and entropy profiles for the four largest relaxed clusters at $z = 1.2$ in physical Mpc. A 100 particle moving average has been used to smooth the data.

unusual feature in the temperature profiles is that the second cluster from the left has a very slightly inverted temperature profile following an extremely strong outflow event. The resulting entropy profile is $S \propto r^{1.7}$, while the remaining profiles all match the $S \propto r^{1.1}$ profile reported elsewhere (*e.g.* Voit, Bryan & Kay 2005).

5. DISCUSSION & CONCLUSIONS

We have presented results from a suite of cosmological simulations that self-consistently follow the evolution of quasars and the outflows associated with them. By tracking the merger history of halos and applying the quasar model of Wyithe & Loeb (2003), we have been able to make direct predictions for the spatial distribution and luminosity function of these objects. Our results are in excellent agreement with the observed correlation function of quasars on both small and large scales, reproducing both the power-law behavior measured by the 2DF redshift survey on ≥ 1 Mpc scales, and the strong break measured from the SDSS on ≤ 1 Mpc scales.

Furthermore, we predict that the quasar-galaxy cross-correlation function should show a small scale up-turn relative to the galaxy-galaxy correlation function. This occurs on sub Mpc scales, and therefore can only be measured from a very large sample of quasars, making its detection difficult even in the large DEEP2 survey. However, it is worth noting that the *Dark Energy Survey* will produce a quasar catalog spanning 5,000 square degrees which combined with photometric redshifts for 300 million galaxies should be able to suppress statis-

tical uncertainties to a sufficiently low level to measure this upturn. We also note that this clustering excess is in qualitative agreement with the increase in the integrated galaxy overdensity at small scales for the SDSS quasar sample (Serber *et al.* 2006). Although the origin of the excess is uncertain, there is an interesting possibility that the presence of an ancillary galaxy can accelerate the merger process via a three-body interaction. Given the extended nature of the mass distribution associated with galaxies it is not clear whether this mechanism will work in a similar way to stellar interactions. We plan to investigate this intriguing idea in the near future.

As the correlation function is dominated by more populous low-luminosity quasars, our spatial results should be largely interpreted as lending support to our dark-matter modeling choice of merger model. Similarly, as it tracks the number of quasars formed as a function of the gas mass accreted onto galaxies, the luminosity function is more sensitive to the details of our feedback modeling. In this case, our simulation qualitatively reproduces the observed anti-hierarchical behavior, but the turn-down is much weaker than observed. Matching the suppression at the brighter end requires that we increase the efficiency of heating from the AGN outflows to mimic that assumed in semi-analytic models. This is equivalent to suppressing one key physical process, namely in-shock cooling in the presence of substructure, and including the ejection of gas from quasar host galaxies. These results emphasize how sensitive the luminosity function is to issues in the baryon physics and how the treatment of these issues

in semi-analytic models is still quite approximate.

Investigation of the mass fractions and filling factors of gas above S_{crit} showed good convergence in the mass fractions at low redshift, but less so in the filling factors. The differences between runs are most noticeable at high redshift, where successively higher resolution leads to the first generation of AGN outflows occurring at earlier epochs. While mass fractions show fairly strong convergence below $z \approx 2$, the tendency of gas above S_{crit} to occupy low overdensity regions makes an accurate calculation of the volume filling factor difficult due to sampling issues. These results are also further complicated by the known dependence of shock resolution on particle number (*e.g.* Thacker *et al.* 2000) where accurate modeling of shock jumps in spherical collapse is reached once $N_{\text{collapse}} > 30,000$. Nonetheless, the results do elucidate that the impact of quasar outflows is largely felt at low redshifts, in agreement with the downsizing trend. Perhaps the most interesting issue we have not yet explored with regards to filling factors is the relative impact of including a more bi-polar outflow. However, there is no reason to expect a difference beyond a factor of two as the gas will flow toward low overdensity regions, as observed in supernova outflow calculations (STD01).

In somewhat denser environments, our results for the cluster $L_X - T$ relation are in broad agreement with observations. This is especially encouraging as our cluster modeling is not as sophisticated as other more targeted studies. In this case, the predominant view is that AGN heating is best modeled in terms of “hot bubble” ejection from the brightest cluster galaxy (BCG) which then mixes with the surrounding material. Interestingly, the exact nature of this mixing is not well understood, and substantial differences are found between Eulerian and Lagrangian simulations, which by definition differ significantly in their treatment of advection. While SPH simulations inhibit the development of instabilities that promote mixing due to the necessary use of flow interpenetration suppression, it has the advantage of exhibiting significantly less numerical diffusion than many Eulerian methods. Ultimately, input from laboratory experiments may well be necessary to help determine the correct mixing behavior. We also note that due to our inefficient star formation model, our simulations include a significant amount of cold gas in BCGs that will tend to promote an “overcooling” instability, which others have avoided by applying phase decoupling (Pearce *et al.* 2000). We believe that this is a significant contributor to the lack of an entropy core in our radial profiles, and removing this central core produces an $L_X - T$ relationship that is significantly less noisy while not exhibiting a large change in normalization at intermediate cluster mass scales. Additionally, the lack of a strong turn-down in the quasar luminosity function at $z = 1.2$ also promotes extremely strong outflows in these clusters that may well be transporting high entropy gas from the core out to the edges of the cluster without significantly raising the entropy of the gas immediately surrounding the BCG.

Perhaps the most intriguing result to come out of our $L_X - T$ study is the prediction that the gas in $z \approx 1$ galaxy groups should be strongly perturbed by AGN activity, which is in the process of turning-off at that epoch. This effect is confined to small and high-redshift clusters for two main reasons. At lower redshifts, the comparative paucity of AGN activity will allow group gas to evolve largely adiabatically, decreasing L_X dramatically to establish the steep $L_X - T$ relation ($L_X \propto T^5$) observed locally. In more massive $z \approx 1$ clusters, on the other hand, the effect of outflows is largely masked when averaging over the material within r_{200} . Thus galaxy groups at $z \approx 1$ represent the key mass and redshift range at which the AGN heating hypothesis is most likely to be testable through observations.

Lastly, our simulation results indicate that simplifications in current semi-analytic models may well be downplaying critical physics. While much attention has been paid to drawing broad conclusions from comparisons between observations and these models, the differences we have uncovered in this investigation are troubling. While, as expected, post processing of our simulation results was able to reproduce the semi-analytic behavior, it is clear that in-shock cooling due to substructure in low-overdensity halos is an issue that must be considered carefully in semi-analytic calculations. Fortunately, constraining the effect by simulation would not be difficult, and ultimately a single parameter could be used to quantify this behavior. On the simulation side, it also is clear that a more detailed understanding of gas ejection from quasar hosts will be necessary for definitive conclusions to be reached. Nonetheless, the insight gained from this initial simulation study clearly serves to highlight the promise of a self-regulating picture of quasar formation. The simple merger model of Wyithe & Loeb (2003), when supplemented with an outflow model, appears to represent a significant step forward in understanding the evolution of quasar clustering and the cause of their anti-hierarchical low-redshift turn-off.

We thank Andrea Ferrara, Piero Madau and Matthias Steinmetz for hosting the IGM-Galaxy Interactions workshop at the KITP where part of this work was undertaken. We are also grateful to Alison Coil, Darren Croton, Marc Davis, Joseph Hennawi & Lars Bildsten for their many useful comments, particularly in regards to our comparisons with observations. Computing was performed at WestGrid (under a RAC grant), SHARCNET and HPCVL. We thank Rob Simmonds of WestGrid for helping arrange a period of dedicated use of their IBM p595 system during initial testing. R.J.T. acknowledges funding from the CITA National Fellow program and NSERC of Canada via the operating grants of Professors Larry Widrow and Richard Henriksen. E.S. was supported by the National Science Foundation under grants PHY99-07949 and AST02-05956.

REFERENCES

- Allen, S. W., Schmidt, R. W. & Fabian A. C. 2002, MNRAS, 334, L11
 Akiyama, M., Ueda, Y., Ohta, K., Takahashi, T., & Yamada, T. 2003, ApJS, 148, 275
 Arnaud, M. & Evrard, E. 1999, MNRAS, 305, 613
 Babul, A., Balogh, M. L., Lewis, G. F., & Poole, G.B. 2002, MNRAS, 330, 329
 Begelman, M. C. & Cioffi, D. F. 1989, ApJ, 345, L21

- Binney, J. 2004, MNRAS, 347, 1093
- Boyle, B. J.; Shanks, T.; Peterson, B. A. 1988, MNRAS, 235, 935
- Boyle, B. J., Shanks, T., Croom, S. M., Smith, R. J., Miller, L., Loaring, N., & Heymans, C. 2000, MNRAS, 317, 1014
- Brandt, W.N., *et al.* 2001, AJ, 122, 2810
- Bryan, G. L., & Norman, M. L. 1998, ApJ, 495, 80
- Boyle, B.J., *et al.* 1998, MNRAS, 296, 1
- Bullock, J. S., Wechsler, R., H., & Somerville, R. S. 2002, MNRAS, 329, 246
- Bundy, K., Ellis, R. S., & Conselice, C. J. ApJ 2005, 625, 621
- Cattaneo, A., Dekel, A., Devriendt, J., Guiderdoni, B., Blaiziot, J. 2006, MNRAS, submitted (astro-ph/06011295)
- Cavaliere, A., Menci, N., & Tozzi, P. 1998, ApJ, 501, 493
- Coil, A. L., Hennawi, J. F., Newman, J. A., Cooper, M. C., & Davis, M. 2006, ApJ, submitted
- Cowie, L. L., Songaila, A., Hu, E. M., & Cohen, J. G. 1996, ApJ, 112, 839
- Cowie, L.L., *et al.* 2003, ApJ, 584, L57
- Croom, S. M., & Shanks, T., 1999, MNRAS, 303, 411
- Croom, S. M., Shanks, T., Boyle, B. J., Smith, R. J., Miller, L., Loaring, N. S., & Hoyle, F. 2001, MNRAS, 325, 483
- Croom, S. M., Shanks, T., Boyle, B. J., Smith, R. J., Miller, L., Loaring, N. S., & Hoyle, F. 2001, MNRAS, 335, 459
- Croton, D. *et al.* 2006, MNRAS, 365, 11
- Couchman, H. M. P., 1991, ApJ, 386, L23
- Davé, R., Hernquist, L., Katz, N., & Weinberg, D. H. 1999, ApJ, 511, 521
- David, L. P., Slyz, A., Jones, C., Forman, W., Vrtilik, S. D., & Arnaud, K. A. 1993, ApJ, 367, 45
- Dekel, A., & Birnboim, Y. 2006, MNRAS, 368, 2
- Di Matteo, T., Springel, V., & Hernquist, L. 2005, Nature, 433, 604
- Eisenstein, D. & Hu, W. 1999, ApJ, 511, 5
- Ellingson, E., Yee, H. K. C., & Green, R. F. 1991, ApJ, 371, 49
- Fan, X., *et al.* 2001, ApJ, 121, 54
- Ferrarese, L. 2002, ApJ, 578, 90
- Finoguenov, A., Bohringer, H., Osmond, J. P. F., Ponman, T. J., Sanderson, A. J. R., Zhang, Y.-Y. & Zimer, M. 2005, preprint (astro-ph/0505419)
- Fontana, A. *et al.* 2004, A&A, 424, 23
- Furlanetto, S., & Loeb, A. 2001, ApJ, 556, 619
- Gebhardt, K. *et al.* 2000, ApJL 539, 13
- Gingold, R. A. & Monaghan, J. J., 1977, MNRAS, 181, 375
- Glazebrook, K. *et al.* 2004, Nature, 430, 181
- Granato, G. L., Silva, L., Monaco, P., Panuzzo, P., Salucci, P. De Zotti, G., & Danese, L. 2001, MNRAS, 324, 757
- Granato, G. L., De Zotti, G., Silva, L., Bressan, A., & Danese, L. 2004, ApJ, 600, 580
- Grossan, B., 1992, PhD thesis, MIT
- Hartwick, F. D. A., & Schade, D. 1990, ARA&A, 28, 437
- Heckman, T. M., Kauffmann, G., Brinchmann, J., Charlot, S., Tremonti, C., & White, Simon D. M. 2004, ApJ, 613, 109
- Helsdon, S.F., & Ponman, T.J. 2000, MNRAS, 315, 256
- Hennawi *et al.* 2006, AJ, 131, 1
- Hernquist, L. 1993, ApJ, 404, 717
- Hopkins, P., Hernquist, L., Martini, P., Cox, T. J., Robertson, B., Di Matteo, T., & Springel, V. 2005a, ApJ, 625, L71
- Hopkins, P., Hernquist, L., Cox, T. J., Di Matteo, T., Martini, P., Robertson, B., Springel, V. 2005b, ApJ, 630, 705
- Hopkins, P., Hernquist, L., Cox, T. J., Di Matteo, T., Robertson, B., Springel, V. 2005c, ApJ, 632, 81
- Hopkins, P., Hernquist, L., Cox, T. J., Robertson, B., Springel, V. 2006, ApJS, 163, 50
- Kaiser, N. 1986, MNRAS, 222, 323
- King, A. 2003, ApJ, 596, L27
- King, A. 2005, ApJ, 635, L121
- Koo, D. C. & Kron, R. G. 1988, ApJ, 325, 92
- Kravtsov, A. V., & Yepes, G. 2000, MNRAS, 318, 227
- La Franca, F., *et al.* 2002, ApJ, 570, 100
- Levine, R. & Gnedin, N. Y. 2005, ApJ, 632, 727
- Levine, R., & Gnedin, N. Y. 2006, ApJL, submitted (astro-ph/0604308)
- Lucy, L. B., 1977, AJ, 82, 1013
- Magliocchetti, M., & Porciani 2003, MNRAS, 346, 186
- Maughan, B. J., Jones, L. R., Ebeling, H. & Scharf, C. 2006, MNRAS, 365, 509
- Menci, N., Fontana, A., Giallongo, E., Grazian, A., & Salimbeni, S. 2006, ApJ, in press (astro-ph/0605123)
- Merritt, D., & Ferrarese, L. 2001, ApJ, 547, 140
- Muanwong, O., Thomas, P. A., Kay, S. T., Pearce, F. R. & Couchman, H. M. P. ApJ, 552, L27
- Nath, B., & Roychowdhury, S. 2002, MNRAS, 333, 145
- Navarro J. F., Frenk C. S., & White S. D. M., 1995, MNRAS, 317, 720
- Nelson, R. P., & Papaloizou, J. C. B. 1994, MNRAS, 270, 1
- Oh, S. P., & Benson, A. 2003, MNRAS, 342, 664
- Ouchi, M. *et al.* 2005, ApJ, 635, L17
- Pearce, F. R., Thomas, P. A., Couchman, H. M. P., & Edge, A. C. 2000, MNRAS, 317, 1029
- Percival, W. J., Scott, D., Peacock, J. A., & Dunlop, J. 2003, MNRAS, 338, L31
- Perlmutter, S., *et al.* 1999, ApJ, 517, 565
- Pei, Y. C. 1995, ApJ, 438, 623
- Piccinotti, G., *et al.* 1982, ApJ, 253, 485
- Ponman, T. J., Sanderson, A. J. R. & Finoguenov, A., 2003, MNRAS, 343, 331
- Pozzetti, *et al.* 2003, A&A, 402, 837
- Rasio, F. A., Pfahl, E. D., & Rappaport, S. 2000, ApJ, 532, L47
- Rees, M., J., & Ostriker, J. P. 1977, MNRAS, 179, 541
- Riess *et al.* 1998, AJ, 116, 1009
- Scannapieco, E., Thacker, R. J. & Davis, M., 2001, ApJ, 557, 605 (STD01)
- Scannapieco, E. & Oh, S. P. 2004, ApJ, 608, 62 (SO04)
- Scannapieco, E. & Thacker, R. J. 2003, ApJ, 590, 69
- Scannapieco, E., Silk, J., & Bouwens, R. 2005, ApJ, 635, L13
- Schmidt, M. & Green, R. F. 1983, ApJ, 269, 352
- Serber, W., Bahcall, N., Menard, B., & Richards, G. 2006, ApJ, 643, 68
- Serna, A., Alimi, J. M., & Chieze, J. P., 1996, ApJ, 461, 884
- Sijacki, D. & Springel, V. 2006, MNRAS, 366, 397
- Silk, J. 1977, ApJ, 211, 638
- Smith, R. J., Boyle, B. J., & Maddox, S. J. 1995, MNRAS, 277, 270
- Spergel, D. N., *et al.* 2003, ApJS, 148, 175
- Springel, V., & Hernquist, L. 2002, MNRAS, 333, 649
- Steffen, A. T., Barger, A. J., Cowie, L. L., Mushotsky, R. F., & Yang, Y. 2003, ApJ, 596, L23
- Sutherland, R. S., & Dopita, M. A., 1993, ApJS, 88, 253
- Thacker, R. J. & Couchman, H. M. P., 2006, Computer Physics Communications, 174, 540
- Thacker, R. J., Tittley, E. R., Pearce, F. R., Couchman, H. M. P. & Thomas, P. A. 2000, MNRAS, 322, 209
- Tozzi, P., Rosati, P., Ettori, S., Borgani, S., Mainieri, V., & Norman, C. 2003, ApJ, 593, 705
- Tremaine, S., *et al.* 2002, ApJ, 574, 740
- Treu, T., Ellis, R. S., Liao, T. X., & van Dokkum, P. G. 2005, ApJ, 622, L5
- Ueda, Y., Ishisaki, Y., Takahashi, T., Makishima, K., & Ohashi, T. 2001, ApJS, 133, 1
- Ueda, Y., Akiyama, M., Ohta, K., & Miyaji, T. 2003, ApJ, 598, 886
- van den Bosch, F. C., Yang, X., & Mo, H. J. 2003, MNRAS, 340, 771
- van Dokkum *et al.* 2004, ApJ, 611, 703
- Vianna, P. T. P. & Liddle, A., 1996, MNRAS, 281, 323
- Voit, G. M., & Bryan, G. L. 2001, Nature, 414, 425
- Voit, G. M., & Donahue, M. 2005, ApJ, 634, 955
- Voit, G. M., Bryan, G. L. & Kay, S. T., 2005, MNRAS, 364, 909
- Wu, K. K. S., Fabian, A. C., & Nulsen P. E. J. 2000, MNRAS, 318, 889
- Wyithe, J. S. B., & Loeb, A. 2002, ApJ, 581, 88
- Wyithe, J. S. B., & Loeb, A. 2003, ApJ, 595, 614
- Wyithe, J. S. B., & Loeb, A. 2005, ApJ, 621, 95
- Zehavi, I. *et al.* 2004, ApJ, 608, 16